www.acsnano.org

Biomimetic Control over Bimetallic Nanoparticle Structure and Activity via Peptide Capping Ligand Sequence

Maichong Xie, Ryuichi Shimogawa, Yang Liu, Lihua Zhang, Alexandre C. Foucher, Prahlad K. Routh, Eric A. Stach, Anatoly I. Frenkel,* and Marc R. Knecht*



Downloaded via UNIV OF PENNSYLVANIA on March 19, 2024 at 16:03:16 (UTC). See https://pubs.acs.org/sharingguidelines for options on how to legitimately share published articles.

Cite This: ACS Nano 2024, 18, 3286–3294



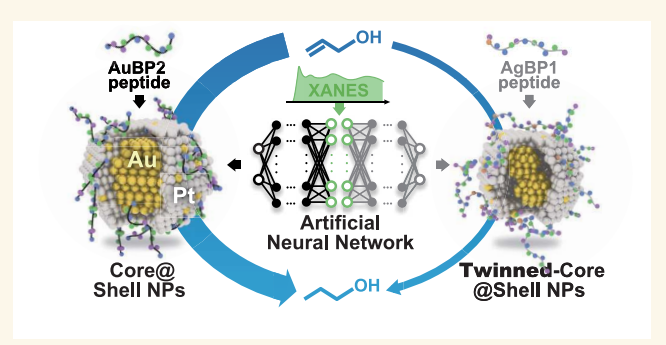
ACCESS

III Metrics & More

Article Recommendations

s Supporting Information

ABSTRACT: The controlled design of bimetallic nanoparticles (BNPs) is a key goal in tailoring their catalytic properties. Recently, biomimetic pathways demonstrated potent control over the distribution of different metals within BNPs, but a direct understanding of the peptide effect on the compositional distribution at the interparticle and intraparticle levels remains lacking. We synthesized two sets of PtAu systems with two peptides and correlated their structure, composition, and distributions with the catalytic activity. Structural and compositional analyses were performed by a combined machine learning-assisted refinement of X-ray absorption spectra and Z-contrast measurements by scanning transmission electron



microscopy. The difference in the catalytic activities between nanoparticles synthesized with different peptides was attributed to the details of interparticle distribution of Pt and Au across these markedly heterogeneous systems, comprising Pt-rich, Aurich, and Au core/Pt shell nanoparticles. The total amount of Pt in the shells of the BNPs was proposed to be the key catalytic activity descriptor. This approach can be extended to other systems of metals and peptides to facilitate the targeted design of catalysts with the desired activity.

KEYWORDS: bimetallic nanoparticles, XAFS, neural network, catalysis, peptides

INTRODUCTION

The rational design of structurally controlled bimetallic nanoparticles (BNPs) is exceedingly important for advanced, sustainable catalysis. In this case, the arrangement of the two metal atoms in the nanoparticle can be a critical factor that leads to changes in the final properties, which can vary substantially based upon the atomic structural arrangement (e.g., alloy vs core@shell). This is especially important for catalysis, where BNPs have demonstrated substantially enhanced reactivity compared to their monometallic counterparts. This enhancement has been observed for numerous catalytic processes and is influenced by the geometric atomic arrangements and, correspondingly, the electronic properties of the reaction active sites at the BNP surface.

The need for improved synthetic methods to control the structure of BNPs is clear. For instance, co-reduction of two metal ions in the presence of a stabilizing ligand has been used for BNP synthesis;^{3–5} however, *a priori* knowledge about the atomic arrangement of the materials produced via this approach remains spotty at both the intraparticle and

interparticle levels. Changes to the ligand are also expected to propagate to the distribution of the resultant heterogeneous structures and reactivity capabilities. Thus, an advanced analysis methodology capable of identifying and estimating the contributions of reactive species (i.e., catalytic active sites), leading to the ability to predict the activity of the material sample that presents a broad compositional heterogeneity, would be invaluable. Such fine structural analysis is critical to understand and help tune and optimize nanoparticle catalytic properties to operate efficiently under sustainable conditions.

As an alternative to conventional syntheses, nature provides pathways for the production of highly controlled materials, at both the atomic level and macroscale; 6-9 these approaches

Received: October 13, 2023 Revised: December 26, 2023 Accepted: January 2, 2024 Published: January 16, 2024

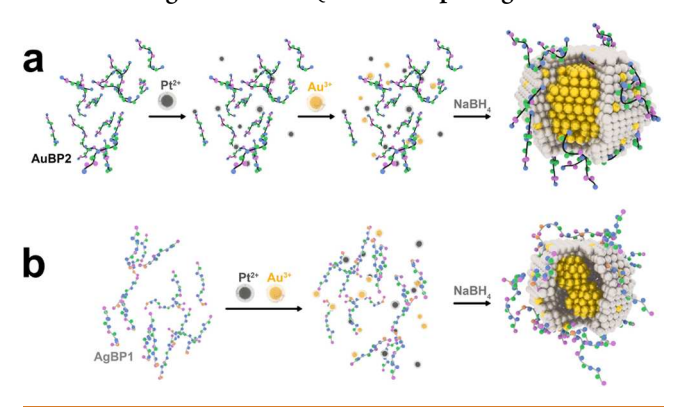




could be translated to prepare structures for technologically important applications. In this regard, peptides have been isolated with affinity for a host of different inorganic material compositions, where the specificity of the binding interaction can be tuned during the biocombinatorial selection process. 10,11 As such, these biomolecules could be engendered with the ability to control the final structure of BNPs based on their inherent material affinity or the nanoparticle synthesis strategy employed. From this fine level of control, peptide/materials binding events could lead to metal surface segregation, changes in the crystallinity of the materials, variations in the bioligand overlayer structure, or other changes in BNP atomic arrangements to control the final particle structure and resultant properties. 12-16 Such ligand capabilities remain attractive but challenging to achieve and require complex surface interactions. Materials-binding peptides, which commonly have 12 residues, represent intriguing ligands to access such capabilities due to their intricate binding patterns spread across the amino acids in the sequence. This level of complexity, which is typically greater than traditional organic ligands, provides a handle to controlling BNP structures.

To probe the ability of peptides to control BNP structures and resultant properties, two different peptides were employed, AuBP2 (WALRRSIRRQSY) and AgBP1 (TGIFKSARAMRN), for the production of PtAu materials (Scheme 1). Both

Scheme 1. Synthetic strategies to generate core@shell BNPs using the (a) AuBP2 and (b) AgBP1 peptides, demonstrating altered core@shell morphologies.



sequences were previously identified with the affinity for noble metals (Au for AuBP2¹⁷ and Ag for AgBP1¹⁸), thus making them ideal sequences to probe structural control capabilities. Interestingly, both peptides were capable of driving the production of Au@Pt core@shell particles, as previously shown for the AuBP2 peptide;¹⁹ however, the catalytic activities for alkene hydrogenation between the two BNPs were substantially different. To this end, the AuBP2-capped materials demonstrated significantly enhanced reactivity compared to the AgBP1-based particles, with maximum reactivity observed for the system prepared at a Pt:Au ratio of 80:20. In both cases, monometallic Pt and Au nanoparticles were also observed, suggesting that changes in either the BNP atomic structure or heterogeneity of the sample, or both, were achieved using the different peptide ligands.

The origin of the marked changes in the activity between the BNPs capped with the two different peptides was elucidated via the correlative use of a recently developed machine learning (ML)-based analysis of X-ray absorption fine structure (XAFS)

data and scanning transmission electron microscopy (STEM) characterization of the BNPs. The increase in reactivity can be attributed to several factors (e.g., the arrangement of the metal atoms in BNPs and the structure of the peptide ligand layer on the particle surface). Surprisingly, it was found that the key factor responsible for the activity changes was the amount of Pt in the shell of BNPs, whose contribution to XAFS had to be disentangled from the interparticle heterogeneous distributions. Taken together, these results demonstrate the role of heterogeneity in significant structural control of BNPs that can be achieved through the use of peptide-based ligands. This structural effect also leads to modulation of the final materials properties, providing potential routes to the *a priori* design of ligands and synthetic strategies for facile control over BNP structure and function.

RESULTS AND DISCUSSION

To explore the use of peptides to control the BNP structure and properties, two sets of PtAu materials capped with either the AuBP2 or AgBP1 sequences were compared. To easily distinguish between the materials, the samples are denoted as Pt_aAu_b -peptide where a and b represent the number of Pt and Au atoms, respectively, out of 100 total metal atoms, and peptide indicates the sequence used to cap the particles (e.g., Pt₅₀Au₅₀-AgBP1 prepared in this work). The AuBP2-capped PtAu BNPs were previously prepared and fully characterized. 19 For the AgBP1-based materials, an altered synthetic approach was employed, as compared to the AuBP2-based synthesis (Scheme 1), where the metal ions were immediately coreduced in the presence of the biomolecule. In this method, a stable colloidal suspension of BNPs was prepared at different Pt:Au ratios. Significant attempts were made to identify a nanoparticle synthesis method that generated stable materials with both peptides; however, such an approach could not be

Initially, the AgBP1-based BNP synthesis was monitored via UV-vis spectroscopy. Figure 1a presents the analysis of the

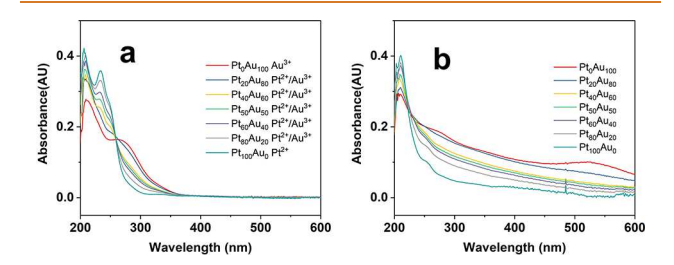


Figure 1. UV—vis analysis of the AgBP1-based BNP synthesis (a) before and (b) after reduction. Clear LMCT bands associated with the metal ions are observed prior to NaBH₄ addition, which were not present in the reduced nanoparticles.

materials prepared at the different Pt:Au ratios prior to reduction (e.g., peptide/Pt²+/Au³+ complexes). Two peaks were present in the sample: one at 232 nm arising for the Pt—Cl ligand to metal charge transfer (LMCT) band and one at 268 nm for the Au—Cl LMCT. For the Au—Cl LMCT, this peak was slightly blue-shifted due to the acidic pH of the system (pH = 4.13). In both cases, the intensity of the observed LMCT increases as the amount of the specific metal increases in the reaction mixture, as anticipated, concomitant with an isosbestic point at 259 nm. Analysis of the materials after reduction, as shown in Figure 1b, demonstrated

significant changes. In general, both LMCT bands for the two metal salts were no longer observed in any sample, and a gradual increase in absorbance toward lower wavelengths was noted, consistent with the production of BNPs. 22 Overall, the intensity of the absorbance was directly proportional to the amount of Au present in the sample. For the $Pt_0Au_{100}\text{-}AgBP1$ material, specifically, a plasmon resonance at 530 nm was noted.

To image the AgBP1-capped PtAu BNPs, STEM analysis of the different structures was performed (Figure 2). The

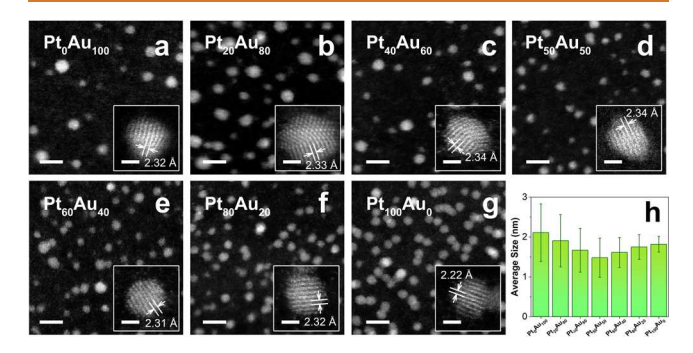


Figure 2. STEM analysis of AgBP1-capped BNPs. Parts (a)-(g) present the STEM image of the indicated BNP composition (scale bar = 5 nm). Lattice-resolved images of a nanoparticle are presented in the inset (scale bar = 1 nm). Part (h) compares the particles size distributions for the different samples.

particles were generally spherical in morphology, where their sizes were calculated by measuring the diameter of at least 500 individual nanoparticles for each sample. For the Pt₀Au₁₀₀-AgBP1 sample, as shown in Figure 2a, an average size of 2.1 \pm 0.7 nm was determined where the sample was highly crystalline. Analysis of the lattice fringe spacing gave a value of 2.32 Å, which is close to the reported value for the Au $\langle 111 \rangle$ plane (2.35 Å).²³ As the amount of Pt in the BNP increased (Figure 2b-d), the size of the particles generally decreased (Figure 2h), reaching a minimum size of 1.5 \pm 0.5 nm for the Pt₅₀Au₅₀-AgBP1 sample; however, after this point, a slight increase in particle size was noted (Figure 2e-g), reaching a size of 1.8 \pm 0.2 nm for the Pt₁₀₀Au₀-AgBP1 materials (Figure 2g). It should be noted that the error bars associated with these measurements suggest that the particle size distributions for the nanoparticles at all concentrations largely overlapped (Figure 2h). For all of the BNP samples, highly crystalline materials were observed with lattice spacings comparable to those for the pure Au sample; however, for the pure Pt materials, a lattice space of 2.22 Å was noted. This spacing was similar to the value for the Pt $\langle 111 \rangle$ plane $(2.27 \text{ Å}).^{24}$ The STEM images also showed the presence of twinning in the nanoparticles, which is expected to disrupt the periodicity of the lattice in PtAu nanoparticles. When comparing the AgBP1capped materials to the AuBP2-capped PtAu BNPs prepared at the same Pt:Au ratios published previously, 19 the sizes of the AgBP1-based structures were similar, albeit somewhat smaller. For the AuBP2-based BNPs, their sizes ranged from 2.1 to 3.7 nm with no evident compositional effects on size.

The nanostructure of the AgBP1-capped BNPs was further analyzed by XAFS. Conventional extended XAFS (EXAFS) analysis is limited for Pt—Au systems due to the overlapping X-ray absorption edges. Moreover, even if the EXAFS signals of two elements could be disentangled, the backscattering

between two elements with close Z numbers is too similar that it cannot be distinguished by EXAFS. 25-27 In previous work, we developed a neural-network (NN)-based method for analyzing the Au L3- and Pt L3-edge XANES data. In that work, STEM-EDS imaging was used to validate the NN-XANES analysis, which demonstrated that the coordination numbers (CNs) of Pt-Au, Pt-Pt, Au-Au, and Au-Pt could be interpreted in terms of the coexistence of two types of AuBP2-capped nanoparticle species: Pt particles/clusters (below 1 nm in size) and/or larger PtAu BNPs with intraparticle heterogeneous distribution. Furthermore, for the BNPs, it was proposed that the intraparticle compositional motifs were consistent with the Au@Pt core@shell structures.

The same neural network developed in the previous work for the AuBP2-stabilized PtAu particles was now deployed to analyze the Au L3-edge and Pt L3-edge XANES spectra of the AgBP1-capped BNPs. The results for the Au-Au, Au-Pt, Pt-Au, and Pt-Pt first nearest neighbor CNs are given in Table S1. The combination of high CN_{Pt-Pt} and CN_{Au-Au} values relative to the CN_{Pt-Au} and CN_{Au-Pt} values indicates that significant heterogeneity exists in these samples, as well. In this work, the previous qualitative method¹⁹ for merely detecting the heterogeneous distribution of two types (Pt-rich and PtAurich) of nanoparticles was extended to a much more general situation in which we characterize the size distributions, molar fractions, and interparticle compositional distributions in the three groups of species: Pt-rich, Au-rich, and PtAu-rich particles. XAFS has been used extensively for the speciation of multiple components of catalysts in time- and temperatureresolved experiments (i.e., when a sequence of spectra with the same components but varying mixing fractions was available, the speciation). 28-30 "Mapping" of the ensemble-averaged data on complex distributions of multiple coexisting species is, however, an ill-posed problem. We have demonstrated before that one can, in principle, set the bounds of variations of structural and compositional descriptors for each species.³¹ In that work, however, it was performed for only two types of species: Rh-rich and Rh-Au-rich ones.

The ensemble can be approximated as a combination of $X_{\rm AV}$, and $X_{\rm AP}$ fractions of Au-rich, Pt-rich, and PtAu-rich nanoparticles, respectively (Figure 3). It is also assumed, for simplicity, that the average sizes of each type of nanoparticle are $D_{\rm AV}$, $D_{\rm PV}$, and $D_{\rm APV}$, respectively. As observed by HR-STEM imaging (Figure 4), the FCC lattice of the BNPs is disrupted at twin boundaries, effectively introducing a "surface", thus lowering the CN value. As such, the effects of the twinning and preferred surface location of Pt atoms, confirmed by EDS

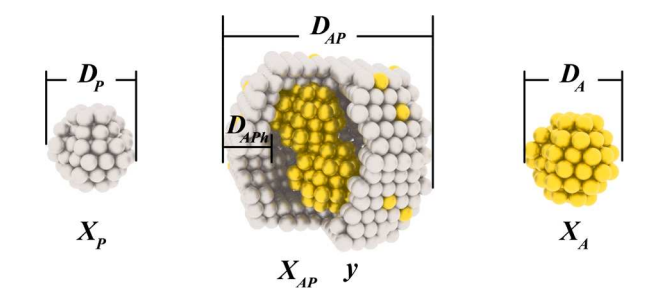


Figure 3. Schematic representation of three different nanoparticle systems (Au-rich, Pt-rich, and AuPt-rich) with their mixing fractions (X) and bimetallic component ratio (y) being used as variables in eqs 1-6.

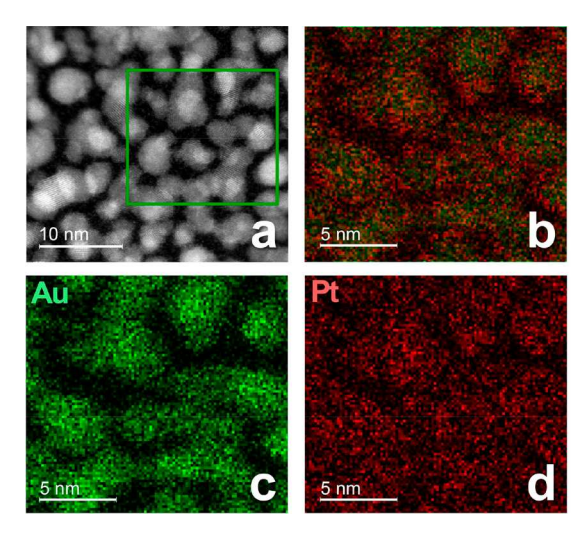


Figure 4. Elemental EDS mapping of the $Pt_{40}Au_{60}$ -AgBP1 BNPs. Part (a) presents the large-field STEM image of the sample, while part (b) displays the overlap between the Pt and Au regions in the sample. Part (c) shows the Au regions of the sample, while part (d) demonstrates the Pt region in red. Those indicate that the Pt component is preferentially on the BNP surface, and the Au section exists as the twinned structure.

mapping (Figure 4), were taken into account in the model. 32,33 BNPs were visualized using a cuboctahedral structure with a hollow sphere of diameter $D_{\rm APh}$ (necessitated by the lack of registry between the twinned regions in the core and the shell) and a Pt-rich shell. Another important parameter is y, the concentration of Au in the BNP. As a result, the ensemble-averaged CNs obtained by NN-XANES analysis can be framed in terms of these parameters (eqs 1–4), of which the values of $X_{\rm A}$, $X_{\rm P}$, $X_{\rm AP}$, and y are of main interest:

$$n_{A-A} = n_{A-A,AP} \left(\frac{X_{AP}}{X_A + X_{AP}} \right) + n_{A-A,A} \left(\frac{X_A}{X_A + X_{AP}} \right)$$
 (1)

$$n_{P-P} = n_{P-P,AP} \left(\frac{X_{AP}}{X_P + X_{AP}} \right) + n_{P-P,P} \left(\frac{X_P}{X_P + X_{AP}} \right)$$
(2)

$$n_{A-P} = n_{A-P,AP} \left(\frac{X_{AP}}{X_A + X_{AP}} \right) \tag{3}$$

$$n_{P-A} = n_{P-A,AP} \left(\frac{X_{AP}}{X_P + X_{AP}} \right)$$
 (4)

In eqs 1–4, the coordination numbers n with subscripts A–A, P–P, A–P, and P–A pertain to specific types of nanoparticles denoted by the second index (A, P, and AP). There is a direct connection between those n values, the corresponding particle diameters (D), and the numbers of atoms (N) in the A, P, and AP types of particles (see Supporting Information, Section S3). This important to note that average particle diameters obtained by XAS measurements are intrinsically weighted with particle volumes (because the number of absorbing atoms grows as the cube of the particle size distributions obtained by STEM analysis (Figure 2) are not weighted. To reconcile between the two measurements, XAS and STEM, volume weighting was applied to correct the particle size distribution observed in STEM measurements for

estimating D (see Supporting Information, Section S4). Considering the atomic balances of Au and Pt atoms in individual NPs, a relationship was derived between the sample average CNs (eq 5, see Supporting Information, Section S5) and the composition of the BNPs, y (eq 6, see Supporting Information, Section S6):

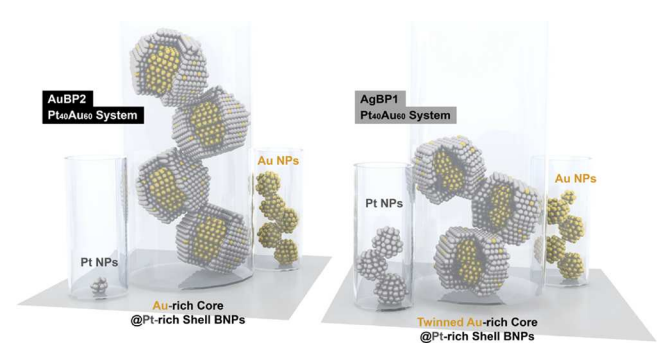
$$\frac{n_{P-A}}{n_{A-P}} = \frac{X_A N_A + y X_{AP} N_{AP}}{X_P N_P + (1-y) X_{AP} N_{AP}}$$
(5)

$$y = \frac{n_{P-A,AP}}{n_{A-P,AP} + n_{P-A,AP}} \tag{6}$$

For this system of nonlinear eqs 1-6, there is no single solution, but a range of solutions that can be identified, depending on the assumptions made of the distribution of particle sizes and their fractions. We also applied an additional assumption, $X_A > X_{AP}$, reflecting a simple fact that the hollow spheres of BNPs are actually filled with twinned Au nanoparticles. The results of this approach are shown in Tables S3-S6 and Figures S3-S14 in the Supporting Information. They confirm the hypothesis about the heterogeneity of Au and Pt distribution because the predicted range of y values (Au concentration) in Pt20Au80-AgBP1 (average y = 0.24) is lower than the ensemble-average Au concentration of 0.65, calculated from the sample-average CNs (see Supporting Information, eq S27). In addition, these results also show that $X_A * N_A$ is greater than $X_P * N_P$, indicating a greater contribution of Au-rich vs Pt-rich nanoparticles. For $Pt_{40}Au_{60}$ -AgBP1, the y values (average y = 0.12) are more similar to those calculated from the sample-average CNs (0.20). The $X_A * N_A$ was estimated to be lower than the $X_P * N_P$, indicating a greater contribution of Pt-rich nanoparticles in that sample.

These results can thus be used to glean fine details about the individual components of this system, paying particular attention to the bimetallic phase. Previous samples with AuBP2 systems (Pt₂₀Au₈₀-AuBP2 and Pt₄₀Au₆₀-AuBP2)¹⁹ were similarly calculated. For all samples studied, y showed low values (<0.5), indicating the PtAu phase of the hollow shell structure is Pt rich, which is consistent with the EDS line scans of Pt₂₀Au₈₀-AuBP2 and Pt₄₀Au₆₀-AuBP2. 19 $n_{\text{P-M},\text{AP}} > n_{\text{A-M},\text{AP}}$ in the bimetallic phase (see Supporting Information, Tables S2– S5), consistent with a model in which the less coordinated atoms (Au) are more preferentially found on the surface of the BNPs compared to Pt.²⁵ Because EXAFS is an average technique, the atoms on or near the nanoparticle surface (i.e., those atoms that have relatively fewer neighbors than those in the bulk of the nanoparticle) have, on average, a smaller metal-metal coordination number than their bulk counterparts. In our model, Au atoms can also preferably be located at the twin boundaries, which will also have lower CNs. There was a noticeable difference in the fraction of the Pt atoms in the shell of BNPs (J, definition given in Supporting Information, eq S28) with different peptide ligands, where Pt atoms preferred to distribute more to BNPs with AuBP2 $(Pt_{20}Au_{80}: 0.96, Pt_{40}Au_{60}: 0.97)$ than AgBP1 $(Pt_{20}Au_{80}: 0.90,$ Pt₄₀Au₆₀: 0.68). To briefly summarize (Scheme 2), the conclusions stemming from this correlated XAFS-TEM analysis are: (1) particles with different compositions should coexist, whereas (2) the bimetallic subphase should have, on average, a thick hollow shell model with a Pt-rich environment,

Scheme 2. Effects of the peptide employed (AuBP2, left; AgBP1, right) on the intra- and interparticle distributions of Pt and Au resulting in the larger and smaller, respectively, numbers of Pt atoms in the BNP shells.



and (3) the Pt atoms tend to distribute more to the BNPs for AuBP2 peptides compared to AgBP1.

EDS mapping results, which were not used in arriving at the model described above, were also in full agreement with the structural conclusions. First, the heterogeneity of the Pt and Au distribution was evident through EDS elemental maps over many PtAu BNPs of different sizes that clearly show the colocalization of Pt and Au in the nanoscale particles (Figure 4). Second, from representative EDS mapping images, the size of the nanoparticle measured in the Pt map is always larger than the size in the Au map, indicative of the Au-core, Pt-richshell motif for the BNPs. These results are fully consistent with the predictions from the XANES analysis. Based upon these characterization methods of the AgBP1-capped PtAu BNPs, a Au@Pt core@shell structure was observed to be dominant for the BNP phase. The monometallic Au and Pt nanoparticles that were present in the sample were predicted to be either small (<1 nm) or quite low in abundance, which is the why such materials were not directly observed in the STEM measurements. Although the structures of the BNPs were similar to the materials prepared from the AuBP2 peptide, 19 disentanglement of the interparticle distribution predicted that Pt favors more to be in the PtAu phase for the AuBP2 than the AgBP1 peptide, which otherwise cannot be analyzed by STEM or XAS measurement by itself.

This difference in Pt distribution between the BNPs capped with the two different peptides (AuBP2 and AgBP1) was interesting and likely affected by the binding events at the particle surface as well as the synthetic mechanism driven by the two different peptides. For the AgBP1 sequence, a direct synthesis was used where the Pt2+ and Au3+ ions were mixed simultaneously with the peptide and subsequently reduced after 15 min. For this reaction, a metal:peptide ratio of 0.5 was employed; whenever a higher ratio was used, rapid bulk material precipitation was evident. Interestingly, when the same successful synthetic strategy for AgBP1 was applied using AuBP2 as the capping ligand, precipitation of bulk materials was evident. For the AuBP2 peptide, an alternative synthetic approach was required that used a metal:peptide ratio of 1 wherein the Pt^{2+} ions were incubated with the peptide for 72 h. After this time, Au3+ ions were added to the system and subsequently reduced after 15 min. This process resulted in the high incorporation of Pt in the PtAu phase.

These differences in the required synthetic strategies to generate the stable materials likely are a result of the binding event between the peptides, metal ions, and the eventual metallic surface of the final particle. For AuBP2, the 72 h incubation period is required for PtCl₄²⁻ hydrolysis to generate PtCl₂(H₂O)₂, which has been shown to bind to the amines of the molecule.³⁶ In this process, after reduction, this binding between the peptide and Pt2+ complexes may facilitate the incorporation of the Pt metal to the surface of the Au@Pt structure. For AgBP1, direct coreduction of the metal ions after a 15 min incubation period with the peptide may result in a lower fraction of Pt in the PtAu phase. In this situation, minimal interactions between the peptides and Pt2+ ions are anticipated, as the dominant species in the mixture was $PtCl_4^{2-}$. As such, the interaction of the peptides with the metal ions appears to be critical for controlling the process. It is important to note that incubating the AgBP1 peptide with the Pt²⁺ ions for 72 h resulted in bulk precipitation, confirming that the sequence is highly critical in not only controlling the material structure but also the specific synthesis driven by the biomolecule.

It is possible that changes in the affinity of the peptide for Pt or Au could give rise to different synthesis mechanisms and even different incorporation fractions of Pt into the BNPs. In this case, the metal for which the peptide has higher affinity should be presented at the surface. Interestingly, quartz crystal microbalance (QCM) analysis of the binding event of the AgBP1 on both Pt and Au demonstrated stronger affinity of the former, while AuBP2 has a reverse trend (Supporting Information, Table S7). This suggests that the raw affinity of the biomolecules for the two different metals plays a minor role in controlling the overall BNP structure.

With the confirmation of the differences in the incorporation fraction of Pt in the PtAu phase for the two different peptide systems, the reactivity of the individual materials was assessed by using olefin hydrogenation. From these structural variations, differences in catalytic reactivity are anticipated. For the reaction, the BNPs were bubbled in solution with $\rm H_2$ gas, after which the olefinic substrate was added. Aliquots were removed from the reaction at selected time points and quantified by GC. ^{37–39} Figure 5a presents the GC analysis for the hydrogenation of allyl alcohol to 1-propanol catalyzed by the Pt₈₀Au₂₀-AuBP2 materials. As is evident, clear separation of the starting material and product was achieved with no evidence of isomer formation.

Using the GC data, reaction quantification was possible. Figure 5b presents this analysis for the reaction catalyzed by using Pt₈₀Au₂₀-AuBP2. Over the 1 h reaction time frame, the allyl alcohol substrate was consumed linearly concomitant with the production of the 1-propanol product. From these data, calculation of the turnover frequency (TOF) of the reaction can be achieved. For this analysis, the TOF value was normalized based upon the total metal concentration, consistent with prior studies. 38-40 Figure 5c presents a plot of the TOF values as a function of the Pt:Au ratio used for BNP production. When considering the BNPs capped using the AgBP1 peptide, negligible to no reactivity was observed for the $Pt_0Au_{100}\text{-}AgBP1$ and $Pt_{20}Au_{80}\text{-}AgBP1$ nanoparticles, as anticipated. When the Pt₄₀Au₆₀-AgBP1-capped BNPs catalyzed the reaction, a TOF value of 152.4 \pm 40.9 mol product/(mol metal \times h) was observed that linearly increased to 288.1 \pm 66.2 mol product/(mol metal \times h) for the Pt₆₀Au₄₀-AgBP1 materials. At higher Pt:Au ratios, no further reactivity enhancement was noted for this system.

When the reactivity of the AuBP2-capped PtAu BNPs was analyzed for the same reaction, significantly enhanced results

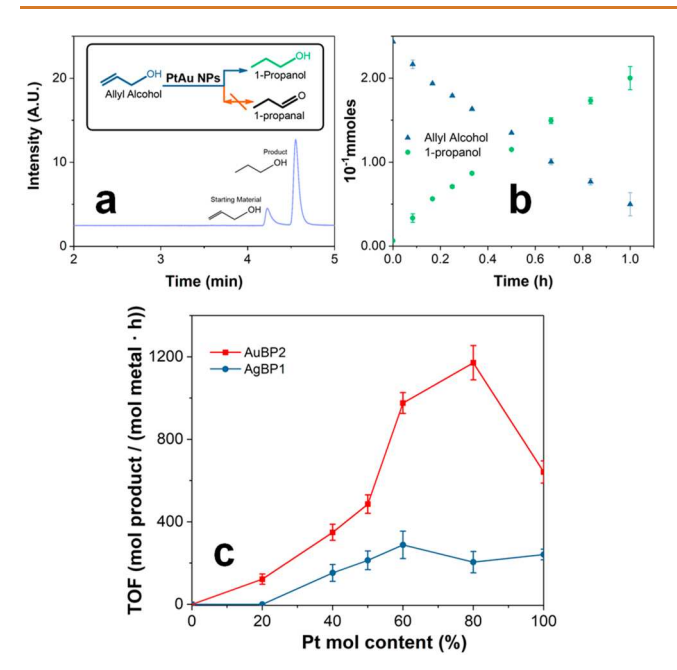


Figure 5. Catalytic analysis of the peptide-capped BNPs for the hydrogenation of allyl alcohol to 1-propanol. Part (a) presents the reaction catalyzed by GC using Pt₈₀Au₂₀-AuBP2. Part (b) displays product generation and substrate consumption as a function of time for part (a), while part (c) shows the observed TOF values for the different peptide-capped BNPs based upon Pt composition.

were observed. For instance, while the $Pt_{20}Au_{80}$ -AgBP1 demonstrated negligible reactivity, notable catalytic turnover was observed for the $Pt_{20}Au_{80}$ -AuBP2 (TOF = 122.2 \pm 25.1 mol product/(mol metal \times h)). As the amount of Pt in the AuBP2-based sample increased, substantially enhanced reactivity was noted, maximizing at a TOF of 1171.1 \pm 83.1 mol of product/(mol of metal \times h) for the reaction catalyzed with the $Pt_{80}Au_{20}$ -AuBP2 structures. This represents a 4-fold enhancement in reactivity as compared to the most reactive BNP for the AgBP1 system. When the $Pt_{100}Au_0$ -AuBP2 materials were used to catalyze the reaction, a diminished TOF of 641.6 \pm 53.8 mol product/(mol metal \times h) was observed.

The observed changes in catalytic reactivity between the BNPs capped with AuBP2 and AgBP1 directly correlate with the anticipated Pt fraction in the PtAu phase. To this end, significantly enhanced reactivity was noted from the Au@Pt BNPs prepared with the AuBP2 peptide, which demonstrated greater Pt incorporation into the bimetallic phase. When the Pt metal favors to be present in monometallic nanoparticles, as observed with the AgBP1-capped materials, substantially diminished catalytic reactivity was indicated. Catalytic turnover similar to that of the pure Pt monometallic nanoparticles was evident from these materials, suggesting that a higher prevalence of monometallic Pd materials was present in this sample. Interestingly, when comparing the two purely monometallic Pt nanoparticles (Pt₁₀₀Au₀-AuBP2 and Pt₁₀₀Au₀-AgBP1), a greater TOF was noted for the AuBP2 system. This suggests that the surface orientation of the peptides on the particles also plays a critical role in controlling the nanoparticle reactivity. In this system, the AuBP2 peptide must be bound in a specific fashion to facilitate substrate accessibility to the catalytic surface to drive the reaction.

It is interesting to note that significantly enhanced reactivity was observed for the $Pt_{60}Au_{40}$ -AuBP2 and $Pt_{80}Au_{20}$ -AuBP2

BNPs as compared to the Pt₁₀₀Au₀-AuBP2 monometallic materials. This suggests that some type of catalytic enhancement was observed from the BNPs; however, prior results from Crooks and colleagues have demonstrated that such effects were not noted for PtAu BNPs with an alloyed structure.⁴¹ Typically, BNPs, such as those composed of PdAu, demonstrate enhanced reactivity due to electronic effects making the system more reactive. 13,16,42 Crooks and colleagues reasoned that such effects were not observed in the PtAu alloy system due to the binding energy of H atoms on the surface. For the AuBP2-capped BNPs studied here, enhanced reactivity likely arises from their Au@Pt structure. In this case, the majority of the Pt metal is pushed to the particle surface to facilitate the reaction, while catalytically unreactive Au is sequestered at the core. In addition, Au is slightly more electronegative than Pt, 43 thus potentially making the surface metal more reactive.

With an understanding of the effects of the peptide passivant and material composition on the catalytic reactivity of the BNPs, the reactivity of the most active system (Pt₈₀Au₂₀-AuBP2) was further explored. The effects of substrate structure were probed over three different alkyl-based reagents (Supporting Information and Table S8). As discussed above, from this analysis using a substrate of allyl alcohol, a TOF value of 1171.1 \pm 83.1 mol product/(mol metal \times h) was observed. When the substrate was changed to either 3-buten-1ol or 4-buten-1-ol, altered catalytic reactivity was noted: 761.3 \pm 22.6 mol product/(mol metal \times h) for 3-buten-1-ol and $1199.6 \pm 54.9 \text{ mol product/(mol metal} \times \text{h)}$ for 4-penten-1-ol. This suggests that the system was sensitive to the length of the alkyl chain in the substrate. Additionally, the materials demonstrated a significant degree of recyclability for continuous use (Supporting Information and Figure S17). In this regard, the first reaction for allyl alcohol hydrogenation reached completion in ~ 160 min. When the same $Pt_{80}Au_{20}$ -AuBP2 BNPs were employed for a second cycle, they achieved complete allyl alcohol turnover within ~300 min. Interestingly, the same length of time (300 min) was required for reaction completion after the third and fourth cycles. This demonstrates that the materials were generally recyclable, even though some degree of reactivity was lost after the first reaction. This loss may be due to structural changes to the BNP surface during the first reaction; similar results have been observed for other nanoparticle catalysts.44,45

Beyond alkenes, $Pt_{80}Au_{20}$ -AuBP2 BNPs were tested for their ability to drive alkyne hydrogenation. For this reaction, the same catalytic process was employed using 3-methyl-1-pentyn-3-ol as the substrate. Figure 6a presents the anticipated mechanism in which 3-methyl-1-penten-3-ol was the alkene intermediate produced en route to the generation of the 3methyl-3-pentanol final product. When the reaction was processed using this alkyne substrate, catalytic turnover was slow (Figure 6b); after 1 h of reaction, only 28.8% of the substrate was converted to the intermediate. The intermediate did grow in concentration throughout the reaction; however, the final alkane product was also observed in the reaction mixture. This suggests that the conversion of both the alkyne and alkene occurred on the particle surface simultaneously, which could contribute to the diminished reactivity for the initial substrate.

To understand the alkyne catalytic process, the simultaneous reduction of both 3-methyl-1-pentyn-3-ol and allyl alcohol was studied (Figure 6c). Using this reaction system, significantly

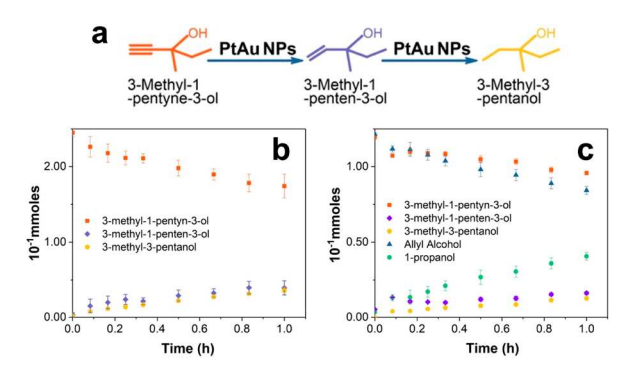


Figure 6. Alkyne hydrogenation catalyzed by $Pt_{80}Au_{20}$ -AuBP2 BNPs. Part (a) presents the reaction mechanisms, while part (b) shows the reaction progression for the alkyne substrate alone. Part (c) displays the competition study for the hydrogenation of both the alkyne and allyl alcohol simultaneously.

diminished turnover of the allyl alcohol was observed, indicating that the alkyne-based catalysis interfered with the reaction. This suggests that the alkyne may be more strongly interacting with the BNP surface, thus blocking active sites to prevent reactivity. This also may play a role in the slower reactivity of the alkyne, whereby it is adsorbed to the particle surface for longer times. Such results are consistent with prior studies that demonstrated similar alkyne effects. ^{39,46}

CONCLUSION

In conclusion, these results demonstrate that peptides have the ability to control nanomaterial synthetic distributions based on the interactions between the biomolecules and the individual metallic components. To this end, changes in the global material composition (e.g., bimetallic vs monometallic) and the BNP individual particle atomic arrangement can be achieved via selection of the peptide-based surface passivant. This fine level of control starts at the level of the BNP synthetic mechanism driven by the specific sequence. The changes in the interparticle distribution of BNPs were disentangled via recently developed atomically resolved EXAFS-based methods, which are highly sensitive to both the BNP structure and the solution composition of materials in the sample. Such an approach is quite intriguing and could easily be adapted to other comparable systems. Taken together, these results demonstrate that the complexity of biorecognition and binding events could be exploited to tune the heterogeneity of BNPs, which could be highly important for the generation of materials for applications ranging from energy harvesting and storage to biosensing.

EXPERIMENTAL METHODS

Chemicals. K₂PtCl₄ was obtained from Acros Organics, while HAuCl₄ was purchased from Alfa Aesar. Sodium borohydride (97%) was acquired from Beantown Chemical. Allyl alcohol, 1-propanol, 3-methyl-1-pentyn-3-ol, 3-methyl-1-penten-3-ol, and antifoam SE-15 were obtained from Sigma-Aldrich, while 3-methyl-3-pentanol was obtained from SAFC Supply Solutions. The AuBP2 and AgBP1 peptides were purchased from GenScript and stored at $-80\,^{\circ}$ C. Ultrahigh-purity H₂ gas cylinders were purchased from Airgas. For all experiments, Milli-Q water (18 mΩ·cm, 24.3 °C) was used. All reagents were used as received.

Synthesis of AgBP1-Capped PtAu BNPs. AgBP1-capped PtAu BNPs were synthesized following standard protocols¹⁶ where the Pt:Au ratio was selected at 0:100, 20:80, 40:60, 50:50, 60:40, 80:20, and 100:0. For the system prepared at a Pt:Au ratio of 40:60, 2 mL of

an aqueous 1 mM AgBP1 stock solution was diluted with 2.96 mL of water. Then 4 μ L of 100 mM K₂PtCl₄ and 6 μ L of 100 mM HAuCl₄ were added to the peptide solution. Note that for the metal salt solutions these were both freshly prepared in water. After 15 min, 30 μ L of freshly prepared 100 mM NaBH₄ in water was introduced to drive metal ion reduction, which was allowed to proceed overnight. Changes to the Pt:Au ratio were subsequently used for each different sample where the ratio of total metal ions:peptide:NaBH₄ was 1:2:3.

Characterization. UV—vis analysis was conducted using an Agilent 8453 UV—vis spectrophotometer employing a 2 mm quartz cuvette. Samples were prepared for STEM imaging by drop-casting 5 μ L of the nanoparticle solution onto a carbon-coated copper TEM grid (Electron Microscopy Sciences). STEM analysis was then performed using a JEOL NEOARM microscope operating at 200 kV. For STEM EDS in the NEOARM EDS analysis, the probe current was 150 pA, the condenser lens aperture was 40 μ m, and the camera length was 4 cm. Two JEOL EDS detectors above the sample collected the fluorescent X-rays. The images were displayed with DigitalMicrograph, a software provided by Gatan, Inc. Analysis of >500 individual nanoparticles was used to identify average particle sizes. For quantification of hydrogenation reactivity, an Agilent 7820A gas chromatograph (GC) was used with a DB-ALC1 column and a flame ionization detector (FID), as previously described. 37

XAFS Analysis. XAFS measurements were performed at the ISS (8-ID) beamline at the National Synchrotron Light Source-II (NSLS-II) at Brookhaven National Laboratory. The solution samples were sealed in Kapton tubes with an \sim 5 mm inner diameter and a wall thickness of 0.2 mm. For each sample, 50 scans were collected to improve the data quality. Two samples with different ratios (Pt₄₀Au₆₀, Pt₂₀Au₈₀) were measured at both the Au L₃-edge and Pt L₃-edge, and one sample (Pt₈₀Au₂₀) was measured at the Pt L₃-edge only, due to the too low Au concentration for quality measurements at the Au L₃-edge. The experimental data are shown in the Supporting Information, Figure S18.

Neural Network-XANES Analysis. To quantitatively analyze the experimental XANES data and obtain information about partial CNs of the Pt and Au absorbing atoms, the neural network approach was applied. The same neural network designed and built for solving the structure of BNPs described in ref 19 was used in the current work. The details about the NN architecture, training set construction, structural models of Au, Pt, and Au—Pt nanoparticles, NN validation, and application to predict the CNs of homo- and heterometallic bond coordination numbers, as well as the details of the error analysis, are given in ref 19.

Heterogeneity Analysis. The heterogeneity analysis was performed by solving eqs 1–6 and S1–S3 using Mathematica 12.3 and Python 3.11. The details of the analysis are in the Supporting Information, and the software program and the input files used for this work are available from https://github.com/Ameyanagi/DecomNano.

Catalytic Hydrogenation Reactivity Analysis. All olefin hydrogenation reactions were carried out using an established method with minor modifications. Briefly, 750 μ L of the peptide-capped PtAu BNPs and 20 μ L of antifoam SE-15 were diluted to 25 mL with H₂O in a three-neck round-bottom flask. This solution was then bubbled with ~0.5 L/min of H₂ with a gas dispersion tube for 15 min. Once complete, 25 mL of an aqueous 10 mM allyl alcohol solution was quickly injected into the flask at room temperature to initiate the reaction. During the 1 h reaction, 1 mL aliquots were removed from the system at selected times and quantified to monitor reaction progression via GC analysis. The solution was quickly injected times and quantified to monitor reaction progression via GC analysis.

ASSOCIATED CONTENT

Supporting Information

The Supporting Information is available free of charge at https://pubs.acs.org/doi/10.1021/acsnano.3c10016.

Definitions of variables used in the equations; supplemental relationships between variables; heterogeneity analysis of Pt₂₀Au₈₀ and Pt₄₀Au₆₀; STEM, QCM,

and supplemental catalytic analysis of the AgBP1-PtAu NPs (PDF)

AUTHOR INFORMATION

Corresponding Authors

Anatoly I. Frenkel — Department of Materials Science and Chemical Engineering, Stony Brook University, Stony Brook, New York 11794, United States; Chemistry Division, Brookhaven National Laboratory, Upton, New York 11973, United States; orcid.org/0000-0002-5451-1207; Email: anatoly.frenkel@stonybrook.edu

Marc R. Knecht — Department of Chemistry, University of Miami, Coral Gables, Florida 33146, United States; Dr. J.T. Macdonald Foundation Biomedical Nanotechnology Institute, University of Miami, Miami, Florida 33136, United States; orcid.org/0000-0002-7614-7258; Email: knecht@miami.edu

Authors

Maichong Xie — Department of Chemistry, University of Miami, Coral Gables, Florida 33146, United States; orcid.org/0000-0002-1654-952X

Ryuichi Shimogawa — Department of Materials Science and Chemical Engineering, Stony Brook University, Stony Brook, New York 11794, United States; Mitsubishi Chemical Corporation, Science & Innovation Center, Aoba-ku, Yokohama 227-8502, Japan

Yang Liu – Department of Materials Science and Chemical Engineering, Stony Brook University, Stony Brook, New York 11794, United States

Lihua Zhang — Center for Functional Nanomaterials, Brookhaven National Laboratory, Upton, New York 11973, United States

Alexandre C. Foucher – Department of Materials Science and Engineering, University of Pennsylvania, Philadelphia, Pennsylvania 19104, United States; orcid.org/0000-0001-5042-4002

Prahlad K. Routh — Department of Materials Science and Chemical Engineering, Stony Brook University, Stony Brook, New York 11794, United States

Eric A. Stach — Department of Materials Science and Engineering, University of Pennsylvania, Philadelphia, Pennsylvania 19104, United States; orcid.org/0000-0002-3366-2153

Complete contact information is available at: https://pubs.acs.org/10.1021/acsnano.3c10016

Author Contributions

The manuscript was written through contributions of all authors. M.X. and R.S. contributed equally.

Funding

The work was supported by the National Science Foundation under grants 2203858 (A.I.F.) and 2203862 (M.R.K.).

Notes

The authors declare no competing financial interest.

ACKNOWLEDGMENTS

Electron microscopy analysis of A.C.F. and E.A.S. was supported as part of the Integrated Mesoscale Architectures for Sustainable Catalysis (IMASC), an Energy Frontier Research Center funded by the U.S. Department of Energy, Office of Science, Basic Energy Sciences, under Award #DE-

SC0012573. This research used beamline 8-ID of the National Synchrotron Light Source II, a U.S. Department of Energy (DOE) Office of Science User Facility operated for the DOE Office of Science by Brookhaven National Laboratory under Contract No. DE-SC0012704. This research used Thermo Fisher Talos 200X of the Center for Functional Nanomaterials, which is a U.S. DOE Office of Science User Facility, and the Scientific Data and Computing Center, a component of the Computational Science Initiative, at Brookhaven National Laboratory under Contract No. DE-SC0012704. This work was carried out in part at the Singh Center for Nanotechnology at the University of Pennsylvania, which is supported by the NSF National Nanotechnology Coordinated Infrastructure Program under grant NNCI-2025608. Additional support to the Nanoscale Characterization Facility at the Singh Center has been provided by the Laboratory for Research on the Structure of Matter (MRSEC) supported by the National Science Foundation (DMR-1720530). We thank E. Stavitski and D. Leshchev for assistance with the synchrotron measurements. We are grateful to Dr. Judith C. Yang for discussion of the plans for electron microscopy studies at the Center for Functional Nanomaterials at Brookhaven National Laboratory.

REFERENCES

- (1) Mustieles Marin, I.; Asensio, J. M.; Chaudret, B. Bimetallic nanoparticles associating noble metals and first-row transition metals in catalysis. *ACS Nano* **2021**, *15* (3), 3550–3556.
- (2) Nakaya, Y.; Hayashida, E.; Shi, R.; Shimizu, K.-i.; Furukawa, S. Interstitial Carbon Dopant in Palladium-Gold Alloy Boosting the Catalytic Performance in Vinyl Acetate Monomer Synthesis. *J. Am. Chem. Soc.* **2023**, 145 (5), 2985–2998.
- (3) Peng, X.; Pan, Q.; Rempel, G. L. Bimetallic dendrimerencapsulated nanoparticles as catalysts: a review of the research advances. *Chem. Soc. Rev.* **2008**, *37*, 1619–1628.
- (4) Chen, M.; Kumar, D.; Yi, C.-W.; Goodman, D. W. The promotional effect of gold in catalysis by palladium-gold. *Science* **2005**, *310*, 291–293.
- (5) Lawrence, R. L.; Olagunju, M. O.; Liu, Y.; Mahalingam, K.; Slocik, J. M.; Naik, R. R.; Frenkel, A. I.; Knecht, M. R. Remote controlled optical manipulation of bimetallic nanoparticle catalysts using peptides. *Catal. Sci. Technol.* **2021**, *11*, 2386–2395.
- (6) Faivre, D.; Schuler, D. Magnetotactic bacteria and magnetosomes. Chem. Rev. 2008, 108 (11), 4875–4898.
- (7) Klaus, T.; Joerger, R.; Olsson, E.; Granqvist, C. G. Silver-based crystalline nanoparticles, microbially fabricated. *Proc. Natl. Acad. Sci. U. S. A.* 1999, *96*, 13611–13614.
- (8) Kroger, N.; Lorenz, S.; Brunner, E.; Sumper, M. Self-assembly of highly phosphorylated silaffins and their function in biosilica morphogenesis. *Science* **2002**, *298* (5593), 584–586.
- (9) Scheffel, A.; Gruska, M.; Faivre, D.; Linaroudis, A.; Plitzko, J. M.; Schüler, D. An acidic protein aligns magnetosomes along a filamentous structure in magnetotactic bacteria. *Nature* **2006**, 440 (7080), 110–114.
- (10) Walsh, T. R.; Knecht, M. R. Biointerface structural effects on the properties and applications of bioinspired peptide-based nanomaterials. *Chem. Rev.* **2017**, *117* (20), 12641–12704.
- (11) Walsh, T. R.; Knecht, M. R. Biomolecular material recognition in two dimensions: peptide binding to graphene, h-BN, and MoS_2 nanosheets as unique bioconjugates. *Bioconj. Chem.* **2019**, 30 (11), 2727–2750.
- (12) Chiu, C.-Y.; Li, Y.; Ruan, L.; Ye, X.; Murray, C. B.; Huang, Y. Platinum nanocrystals selectively shaped using facet-specific peptide sequences. *Nat. Chem.* **2011**, *3*, 393–399.
- (13) Merrill, N. A.; McKee, E. M.; Merino, K. C.; Drummy, L. F.; Lee, S.; Reinhart, B.; Ren, Y.; Frenkel, A. I.; Naik, R. R.; Bedford, N.

- M. Identifying the atomic-level effects of metal composition on the structure and catalytic activity of peptide-templated materials. *ACS Nano* **2015**, *9*, 11968–11979.
- (14) Merrill, N. A.; Nitka, T. T.; McKee, E. M.; Merino, K. C.; Drummy, L. F.; Lee, S.; Reinhart, B.; Ren, Y.; Munro, C. J.; Pylypenko, S. Effects of metal composition and ratio on peptidetemplated multimetallic PdPt nanomaterials. ACS Appl. Mater. Interfaces 2017, 9, 8030–8040.
- (15) Slocik, J. M.; Naik, R. R. Biologically programmed synthesis of bimetallic nanostructures. *Adv. Mater.* **2006**, *18*, 1988–1992.
- (16) Bedford, N. M.; Showalter, A. R.; Woehl, T. J.; Hughes, Z. E.; Lee, S.; Reinhart, B.; Ertem, S. P.; Coughlin, E. B.; Ren, Y.; Walsh, T. R. Peptide-directed PdAu nanoscale surface segregation: toward controlled bimetallic architecture for catalytic materials. *ACS Nano* **2016**, *10*, 8645–8659.
- (17) Hnilova, M.; Oren, E. E.; Seker, U. O.; Wilson, B. R.; Collino, S.; Evans, J. S.; Tamerler, C.; Sarikaya, M. Effect of molecular conformations on the adsorption behavior of gold-binding peptides. *Langmuir* **2008**, *24*, 12440–12445.
- (18) Hnilova, M.; Liu, X.; Yuca, E.; Jia, C.; Wilson, B.; Karatas, A. Y.; Gresswell, C.; Ohuchi, F.; Kitamura, K.; Tamerler, C. Multifunctional protein-enabled patterning on arrayed ferroelectric materials. *ACS Appl. Mater. Interfaces.* **2012**, *4*, 1865–1871.
- (19) Liu, Y.; Xie, M.; Marcella, N.; Foucher, A. C.; Stach, E. A.; Knecht, M. R.; Frenkel, A. I. Z-Contrast Enhancement in Au-Pt Nanocatalysts by Correlative X-ray Absorption Spectroscopy and Electron Microscopy: Implications for Composition Determination. ACS Appl. Nano Mater. 2022, 5, 8775–8782.
- (20) Khullar, P.; Singh, V.; Mahal, A.; Kaur, H.; Singh, V.; Banipal, T. S.; Kaur, G.; Bakshi, M. S. Tuning the shape and size of gold nanoparticles with triblock polymer micelle structure transitions and environments. *J. Phys. Chem. C* **2011**, *115* (21), 10442–10454.
- (21) Wang, S.; Qian, K.; Bi, X.; Huang, W. Influence of speciation of aqueous HAuCl₄ on the synthesis, structure, and property of Au colloids. *J. Phys. Chem. C* **2009**, *113*, 6505–6510.
- (22) Creighton, J. A.; Eadon, D. G. Ultraviolet-visible absorption spectra of the colloidal metallic elements. *J. Chem. Soc., Faraday Trans.* **1991**, *87*, 3881–3891.
- (23) Wang, P.; Liu, Z.-G.; Chen, X.; Meng, F.-L.; Liu, J.-H.; Huang, X.-J. UV irradiation synthesis of an Au-graphene nanocomposite with enhanced electrochemical sensing properties. *J. Mater. Chem. A* **2013**, *J.* 9189–9195.
- (24) Chou, H.-l.; Lai, F.-J.; Su, W.-N.; Pillai, K. C.; Sarma, L. S.; Hwang, B.-J. Investigation of Formation Mechanism of Pt (111) Nanoparticle Layers Grown on Ru (0001) Core. *Langmuir* **2011**, 27, 1131–1135.
- (25) Frenkel, A. I. Applications of extended X-ray absorption fine-structure spectroscopy to studies of bimetallic nanoparticle catalysts. *Chem. Soc. Rev.* **2012**, *41* (24), 8163–8178.
- (26) Liu, J.; Amit, Y.; Li, Y.; Plonka, A. M.; Ghose, S.; Zhang, L.; Stach, E. A.; Banin, U.; Frenkel, A. I. Reversed nanoscale Kirkendall effect in Au-InAs hybrid nanoparticles. *Chem. Mater.* **2016**, 28 (21), 8032–8043.
- (27) Menard, L. D.; Wang, Q.; Kang, J. H.; Sealey, A. J.; Girolami, G. S.; Teng, X.; Frenkel, A. I.; Nuzzo, R. G. Structural characterization of bimetallic nanomaterials with overlapping x-ray absorption edges. *Phys. Rev. B* **2009**, *80* (6), 064111.
- (28) Frenkel, A. I.; Kleifeld, O.; Wasserman, S. R.; Sagi, I. Phase speciation by extended x-ray absorption fine structure spectroscopy. *J. Chem. Phys.* **2002**, *116* (21), 9449–9456.
- (29) Piovano, A.; Agostini, G.; Frenkel, A. I.; Bertier, T.; Prestipino, C.; Ceretti, M.; Paulus, W.; Lamberti, C. Time resolved in situ XAFS study of the electrochemical oxygen intercalation in SrFeO₂. 5 Brownmillerite structure: comparison with the homologous SrCoO². 5 system. *J. Phys. Chem. C* **2011**, *115* (4), 1311–1322.
- (30) Wang, Q.; Hanson, J. C.; Frenkel, A. I. Solving the structure of reaction intermediates by time-resolved synchrotron x-ray absorption spectroscopy. *J. Chem. Phys.* **2008**, *129* (23), 234502.

- (31) Duan, Z.; Timoshenko, J.; Kunal, P.; House, S. D.; Wan, H.; Jarvis, K.; Bonifacio, C.; Yang, J. C.; Crooks, R.; Frenkel, A. I.; Humphrey, S. M. Structural characterization of heterogeneous RhAu nanoparticles from a microwave-assisted synthesis. *Nanoscale* **2018**, *10* (47), 22520–22532.
- (32) Frenkel, A. I.; Hills, C. W.; Nuzzo, R. G. A view from the inside: complexity in the atomic scale ordering of supported metal nanoparticles. *J. Phys. Chem. B* **2001**, *105*, 12689–12703.
- (33) Glasner, D.; Frenkel, A. I. In Geometrical Characteristics of Regular Polyhedra: Application to EXAFS Studies of Nanoclusters; AIP Conference Proceedings; American Institute of Physics, 2007; pp 746–748.
- (34) Montejano-Carrizales, J.; Aguilera-Granja, F.; Moran-Lopez, J. Direct enumeration of the geometrical characteristics of clusters. *Nanostruct. Mater.* **1997**, *8* (3), 269–287.
- (35) Frenkel, A. I.; Yevick, A.; Cooper, C.; Vasic, R. Modeling the structure and composition of nanoparticles by extended X-ray absorption fine-structure spectroscopy. *Annu. Rev. Anal Chem. (Palo Alto Calif)* **2011**, *4*, 23–39.
- (36) Knecht, M. R.; Weir, M. G.; Myers, V. S.; Pyrz, W. D.; Ye, H.; Petkov, V.; Buttrey, D. J.; Frenkel, A. I.; Crooks, R. M. Synthesis and characterization of Pt dendrimer-encapsulated nanoparticles: effect of the template on nanoparticle formation. *Chem. Mater.* **2008**, *20* (16), 5218–5228
- (37) Bhattacharjee, S.; Bruening, M. L. Selective hydrogenation of monosubstituted alkenes by Pd nanoparticles embedded in polyelectrolyte films. *Langmuir* **2008**, *24*, 2916–2920.
- (38) Pacardo, D. B.; Ardman, E.; Knecht, M. R. Effects of substrate molecular structure on the catalytic activity of peptide-templated Pd nanomaterials. *J. Phys. Chem. C* **2014**, *118*, 2518–2527.
- (39) Parab, A. D.; Slocik, J. M.; Naik, R. R.; Knecht, M. R. Peptide-Driven Fabrication of Catalytically Reactive Rhodium Nanoplates. *ACS Appl. Nano Mater.* **2018**, *1* (12), 7149–7158.
- (40) Niu, Y.; Yeung, L. K.; Crooks, R. M. Size-selective hydrogenation of olefins by dendrimer-encapsulated palladium nanoparticles. *J. Am. Chem. Soc.* **2001**, *123* (28), 6840–6846.
- (41) Luo, L.; Duan, Z.; Li, H.; Kim, J.; Henkelman, G.; Crooks, R. M. Tunability of the adsorbate binding on bimetallic alloy nanoparticles for the optimization of catalytic hydrogenation. *J. Am. Chem. Soc.* **2017**, *139* (15), 5538–5546.
- (42) Scott, R. W.; Wilson, O. M.; Oh, S.-K.; Kenik, E. A.; Crooks, R. M. Bimetallic palladium- gold dendrimer-encapsulated catalysts. *J. Am. Chem. Soc.* **2004**, *126*, 15583–15591.
- (43) Chou, T. S.; Perlman, M. L.; Watson, R. E. Electronegativity and electron binding in gold alloys. *J. phys. Rev. B* **1976**, *14* (8), 3248.
- (44) Azua, A.; Finn, M.; Yi, H.; Beatriz Dantas, A.; Voutchkova-Kostal, A. Transfer hydrogenation from glycerol: activity and recyclability of iridium and ruthenium sulfonate-functionalized N-heterocyclic carbene catalysts. *ACS Sustain. Chem. Eng.* **2017**, *5* (5), 3963–3972.
- (45) Bhandari, R.; Pacardo, D. B.; Bedford, N. M.; Naik, R. R.; Knecht, M. R. Structural control and catalytic reactivity of peptidetemplated Pd and Pt nanomaterials for olefin hydrogenation. *J. Phys. Chem. C* 2013, *117*, 18053–18062.
- (46) Ballesteros-Soberanas, J.; Carrasco, J. A.; Leyva-Pérez, A. Parts-Per-Million of Soluble Pd⁰ Catalyze the Semi-Hydrogenation Reaction of Alkynes to Alkenes. *J. Org. Chem.* **2023**, *88* (1), 18–26.